Exocometary gas in the HD 181327 debris ring

S. Marino,[1,2,3]⋆ L. Matrà,[1] C. Stark,[4] M. C. Wyatt,[1] S. Casassus,[2,3] G. Kennedy,[1] D. Rodriguez,[2,5] B. Zuckerman,[6] S. Perez,[2,3] W. R. F. Dent,[7] M. Kuchner,[8] A. M. Hughes,[9] G. Schneider,[10] A. Steele,[11] A. Roberge,[8] J. Donaldson[11] and E. Nesvold[12]

[1]*Institute of Astronomy, University of Cambridge, Madingley Road, Cambridge CB3 0HA, UK*
[2]*Departamento de Astronomía, Universidad de Chile, Casilla 36-D Santiago, Chile*
[3]*Millennium Nucleus 'Protoplanetary Disks', Chile*
[4]*Space Telescope Science Institute, 3700 San Martin Dr, Baltimore, MD 21218, USA*
[5]*Department of Astrophysics, American Museum of Natural History, Central Park West at 79th Street, New York, NY 10034, USA*
[6]*Department of Physics and Astronomy, University of California, Los Angeles, CA 90095-1562, USA*
[7]*Joint ALMA Observatory, Alonso de Córdova 3107, 763-0355 Vitacura, Santiago, Chile*
[8]*Exoplanets and Stellar Astrophysics Laboratory, NASA Goddard Space Flight Center, Greenbelt, MD, USA*
[9]*Van Vleck Observatory, Astronomy Department, Wesleyan University, 96 Foss Hill Drive, Middletown, CT 06459, USA*
[10]*Department of Astronomy/Steward Observatory, The University of Arizona, 933 N. Cherry Ave., Tucson, AZ 85721, USA*
[11]*Department of Astronomy, University of Maryland, College Park, MD 230742, USA*
[12]*Department of Terrestrial Magnetism, Carnegie Institution for Science, Washington, DC 20015, USA*

ABSTRACT

An increasing number of observations have shown that gaseous debris discs are not an exception. However, until now, we only knew of cases around A stars. Here we present the first detection of ^{12}CO (2–1) disc emission around an F star, HD 181327, obtained with the Atacama Large Millimeter/submillimeter Array (ALMA) observations at 1.3 mm. The continuum and CO emission are resolved into an axisymmetric disc with ring-like morphology. Using a Markov chain Monte Carlo method coupled with radiative transfer calculations, we study the dust and CO mass distribution. We find the dust is distributed in a ring with a radius of 86.0 ± 0.4 au and a radial width of 23.2 ± 1.0 au. At this frequency, the ring radius is smaller than in the optical, revealing grain size segregation expected due to radiation pressure. We also report on the detection of low-level continuum emission beyond the main ring out to $\sim$200 au. We model the CO emission in the non-local thermodynamic equilibrium regime and we find that the CO is co-located with the dust, with a total CO gas mass ranging between 1.2×10^{-6} M$_\oplus$ and 2.9×10^{-6} M$_\oplus$, depending on the gas kinetic temperature and collisional partners densities. The CO densities and location suggest a secondary origin, i.e. released from icy planetesimals in the ring. We derive a CO+CO$_2$ cometary composition that is consistent with Solar system comets. Due to the low gas densities, it is unlikely that the gas is shaping the dust distribution.

Key words: circumstellar matter – stars: individual: HD 181327 – planetary systems – radio continuum: planetary systems.

1 INTRODUCTION

Recent surveys have shown that at least $\sim$20 per cent of nearby solar-type stars (FGK type) host Kuiper belt analogue debris discs (Hillenbrand et al. 2008; Bryden et al. 2009; Eiroa et al. 2013; Matthews et al. 2014). From multiwavelength observations, we know that they are composed of dust grains in a wide size distribution ranging from µm- to mm-sized grains and collisional models require the presence

of km-sized planetesimals. These large bodies are a byproduct of planet formation and continually replenish the dust population as the result of a collisional cascade (see Wyatt 2008). The orbits of these planetesimals can be drastically perturbed by the presence of planets, and hence the disc density distribution can reveal a hidden planetary system (e.g. Wyatt et al. 1999; Kuchner & Holman 2003). Thus, the study of debris discs is an alternative method to characterize planetary systems and the outcome of planet formation. High-resolution images of debris discs have shown ring-like structures (e.g. HR 4796A; Perrin et al. 2015), warps (e.g. β Pic; Heap et al. 2000), gaps or double ring structures (e.g. HD 107146;

Ricci et al. 2015) and eccentric rings (e.g. Fomalhaut, Kalas et al. 2008), suggesting the dynamical presence of planets shaping the debris spatial distribution.

Optical observations of discs can give insights about the distribution of μm-sized dust grains at the bottom of the collisional cascade, where stellar radiation and stellar winds become significant for the dust dynamics (Thébault & Wu 2008). On the other hand, dust thermal emission at millimetre wavelengths is dominated by big grains (∼0.1–10 mm) for which radiation forces are negligible ($\beta \equiv F_{rad}/F_g \ll 1.0$), tracing the location of the parent bodies. Therefore, millimetre observations are fundamental to study the distribution of the more massive planetesimals at the top of the collisional cascade.

Moreover, in some of these systems, significant amounts of gas has been detected, especially in young debris discs that recently left the protoplanetary disc phase. This gas can potentially impact the dust dynamics and density distribution, producing structures that are usually attributed to perturbing planets (Lyra & Kuchner 2013). The origin of this gas is still under debate; however, recent observations have allowed dynamical studies and thus a more detailed picture. This has favoured a secondary origin scenario in the case of β Pictoris (Dent et al. 2014) and 49 Ceti (Zuckerman, Forveille & Kastner 1995; Zuckerman & Song 2012), in which gas is released from icy bodies, e.g. through destructive collisions or photodesorption. In other systems, the gas seems to be primordial (e.g. HD 21997; Kóspál et al. 2013). However, until now, gas had only been detected in seven debris discs, all of them around A stars (see table 5 in Moór et al. 2015, for a complete list of debris discs with gas detections).

In this work, we study the debris disc around the F5/6 main-sequence star HD 181327 (Nordström et al. 2004; Torres et al. 2006), member of the 23 ± 3 Myr old β Pic moving group (Mamajek & Bell 2014) and located at a distance of 51.8 ± 1.7 pc (van Leeuwen 2007). The star has an infrared (IR) excess with a fractional luminosity of $L_{IR}/L_\star \sim 0.2$ per cent (Lebreton et al. 2012) that comes from dust thermal emission that has been marginally resolved at different wavelengths: at 18.3 μm by Chen, Fitzgerald & Smith (2008) and at 70 μm, 100 μm and 3.2 mm by Lebreton et al. (2012). *Hubble Space Telescope* (*HST*)-scattered light observations resolved a debris ring of μm-sized grains with a peak at ∼90 and 36 au wide (Schneider et al. 2006; Stark et al. 2014). The latter study identified a possible radial dust size segregation due to radiation pressure, based on variations of the scattering phase function with radius. Moreover, they found asymmetries that could be interpreted as an increase in the optical depth in the west side of the ring, potentially due to either a recent catastrophic disruption or warping of the disc by the interstellar medium (ISM).

We present the first the Atacama Large Millimeter/submillimeter Array (ALMA) observations to study the dust continuum at 220 GHz and the CO gas distribution, constrain the location of planetesimals, look for asymmetries that could give hints on the origin of the asymmetric features observed by the *HST*, and study the origin of the CO gas. In Section 2, we present the observations and imaging of the dust continuum and CO line emission. In Section 3, we compare the observations with an axisymmetric disc model for the dust continuum and CO (2–1), using a Markov chain Monte Carlo (MCMC) method coupled with radiative transfer simulations to sample the parameter space and estimate the debris spatial distribution, CO gas mass and the disc orientation in the sky. In Section 4, we discuss the implications of the dust continuum and CO observations, we compare them with the previous *HST* observations, we derive a cometary composition based on the CO observations, and

we discuss scaleheight constrains from ALMA observations of debris discs. Finally, in Section 5, we summarize the main results and conclusions.

2 ALMA OBSERVATIONS AND IMAGING

HD 181327 was observed by ALMA in Band 6 on 2014 March 10 as part of the cycle 1 project 2012.1.00437.S. The total number of antennas was 26 with minimum and maximum projected baselines of 12 and 365 m, respectively. The total time on source excluding overheads was 34 min. Three months later, on June 4 and 12, three new observation runs using the same band were carried out corresponding to the cycle 2 project 2013.1.00523.S. The total number of antennas was 39 with a minimum and maximum projected baselines of 15 and 650 m, respectively. The total time on source excluding overheads was 129 min.

On the first run, J1924-2914 was used as bandpass calibrator, while Titan and J1819-6365 were used as primary flux and phase calibrators, respectively. In the second project, J2056-4714 and J2056-472 were used as bandpass calibrators, with the latter used as primary flux calibrator too. We used J2009-4849 as phase calibrator. Calibrations were applied using the pipeline provided by ALMA.

On both projects, the ALMA correlator provided four spectral windows (spws), three exclusively dedicated to study the dust continuum with 128 channels and a total bandwidth of 2 GHz centred at: 212.9, 214.9 and 228.1 GHz in the first project, and 214.6, 216.6 and 232.5 GHz in the second. The fourth spw was configured with a higher spectral resolution of 244 KHz and total bandwidth of 937.5 MHz (3840 channels), centred at 230.5 GHz to target the ^{12}CO (2–1) transition at 230.538 GHz in both projects. We combine the two data sets from both projects to achieve the most complete $u - v$ coverage and the highest signal-to-noise ratio (S/N) on the reconstructed continuum image and CO line emission.

2.1 Dust continuum

The image synthesis of the dust continuum was carried out using a non-parametric least-squares modelling technique that incorporates a regularization term called 'entropy' from a family of maximum entropy methods (MEMs). Examples of usage of MEM for image synthesis in Astronomy can be found in Pantin & Starck 1996, Casassus et al. 2006, Levanda & Leshem 2010, Casassus et al. 2013, Warmuth & Mann 2013, Coughlan & Gabuzda 2013 and Marino et al. 2015. These deconvolved images 'superresolve' the interferometric data, as the entropy prior allows an extrapolation of spatial frequencies beyond those sampled by the interferometer. We call the whole algorithm uvmem and the resulting images as 'MEM models'. The deconvolved image can then be 'restored' by convolving with a Clean beam corresponding to natural or Briggs weighting and adding the dirty map of the residuals. The restored maps are comparable to standard Clean images. While the resolution or point spread function on the deconvolved image can vary at different locations, the resolution on the restored images is well characterized by a synthetic beam of 0.47 arcsec × 0.36 arcsec and 0.69 arcsec × 0.58 arcsec, corresponding to Briggs and natural weighting, respectively.

In Fig. 1, we present the results of the image synthesis on the continuum emission: (a) MEM model, (b) restored image with Briggs weighting (Briggs map hereafter) and (c) restored image with natural weights (natural map hereafter). To smooth the artefacts due to thermal noise on the visibilities and characterize the noise level in the image space, we perform a Monte Carlo simulation bootstrapping the measured visibilities, i.e. adding a random Gaussian noise
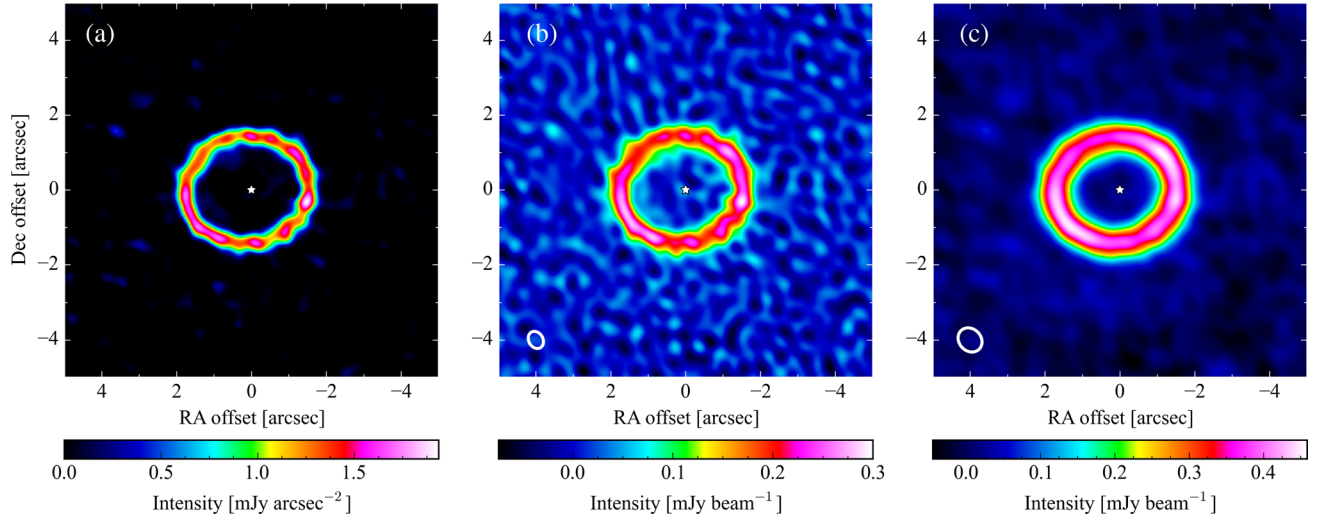
Figure 1. ALMA dust continuum maps at 220 GHz (Band 6). (a) MEM non-parametric model (regularized with the maximum entropy method). (b) Restored image adding residuals and convolving with a synthetic beam corresponding to Briggs weighting (0.47 arcsec × 0.36 arcsec). (c) Restored image adding residuals and convolving with a synthetic beam corresponding to natural weighting (0.69 arcsec × 0.58 arcsec). The respective beams are represented by white ellipses. The *x*- and *y*-axes indicate the offset from the stellar position in RA and Dec. in arcsec, i.e. north is up and east is left. The stellar position is marked with a white star.

according to the observed dispersion on each baseline and repeating the image synthesis described above. The presented images are the median of 200 iterations. We observe a noise level of 0.022 mJy beam^{-1} on the Briggs map, while 0.015 mJy beam^{-1} on the natural map, estimated from the median absolute deviation and from the rms on the dirty map of the residuals. The total flux in the Natural map inside a ellipse of semimajor axis 4 arcsec and oriented as the best-fitting model (see Section 3) is 7.9 ± 0.2 mJy, the error which comes from the image noise and does not take into account the error on the absolute flux calibration (∼10 per cent). This is consistent with the trend of the spectral energy distribution (SED) between 170 µm [Moór et al. 2006, Infrared Space Observatory (ISO)] and 3.2 mm [Lebreton et al. 2012, Australia Telescope Compact Array (ATCA)], but too low compared to the 0.05 Jy at 870 µm observed by LABOCA-APEX (Nilsson et al. 2009), possibly due to a background galaxy in the primary beam. Inside the primary beam, we also detect two compact sources with peak intensities of 0.14 and 0.08 mJy beam^{-1}, located at 8 arcsec with a PA = 9°.5 and 9 arcsec with a PA of 210°, respectively. These are probably background galaxies (see Fig. 9) as the position of the southern compact source is consistent with an edge-on galaxy observed in the STIS/*HST* observations in 2011 (Stark et al. 2014).

Similar to previous observations of scattered light, the disc presents a ring-like morphology. The bulk of the emission is radially confined between ∼50 and 125 au (∼1.0–2.4 arcsec) with a peak intensity at 85.8 ± 0.3 au obtained by fitting an ellipse to the peak intensities along the ring of the MEM model. When we compare these results with the *HST* observations, we find that the ring is slightly narrower and shifted inwards in the millimetre, while the inner edge in scattered light (82.3 ± 1.1) is close to the peak radius in the millimetre. This is consistent with what would be expected from grain size segregation due to radiation pressure, previously suggested in this disc by Stark et al. (2014). Radiation pressure causes small dust grains to extend farther out in radius compared with millimetre grains, shifting the density maximum of small grains to larger radii (see discussion in Section 4.3).

The disc emission appears consistent with an axisymmetric ring and most of the observed intensity variations along the ring in the

panels of Fig. 1 and the small offset from the star can be explained by the PA of the beam, the noise level and the ALMA astrometric error (see Section 4.1). In Section 3.1, we compare with an axisymmetric model.

In Fig. 2, we present intensity profiles of the maps presented in Figs 1(a) and (b), along the ring's major and minor axis, together with the deprojected mean intensity at all azimuths extracted from Fig. 1(c). In the top and middle panels, the MEM model profile is represented by a red line, while the Briggs map profile is represented in blue with blue shaded areas equivalent to $1\sigma = 0.022/\sqrt{2}$ mJy beam^{-1} (the factor $1/\sqrt{2}$ is due to the mean between the opposite sides of the disc). The projected Briggs Clean beam is presented with dashed black lines. The radial extent of the emission both along the major and minor axis is wider than the beam, demonstrating that we can marginally resolve the width of the ring. The full width at half-maximum (FWHM) of the ring is ∼0.5 arcsec, which at a distance of 51.8 pc translates to ∼25 au. A more accurate estimation is presented in Section 3.1. The bottom panel shows that the disc emission extends out to ∼4 arcsec (200 au) in either a second ring or a halo component. The grey area in the bottom panel represents the 99.7 per cent confidence region equivalent to $3\sigma = 0.015/\sqrt{N_{\mathrm{beams}}}$ mJy beam^{-1} (the factor $1/\sqrt{N_{\mathrm{beams}}}$ is due to the mean at all azimuth and the number of independent points). In Fig. 1(c), this emission is also just visible as a broad ring around 4 arcsec. To test the significance of this detection and whether this could be a product of our image synthesis method, we produce Clean images obtaining roughly the same results. Moreover, the second component is recovered in the dirty map of the residuals when a best-fitting ring model is subtracted to the data (see Section 3 for a description of the ring model). A brief discussion about the origin of this emission and the dirty map of the residuals is presented in Section 4.

2.2 ^{12}CO (2–1)

To study the ^{12}CO (2–1) transition line at 230.538 GHz (rest frequency), we first subtract the continuum emission from the visibilities fitting a polynomial of the first order at the frequencies
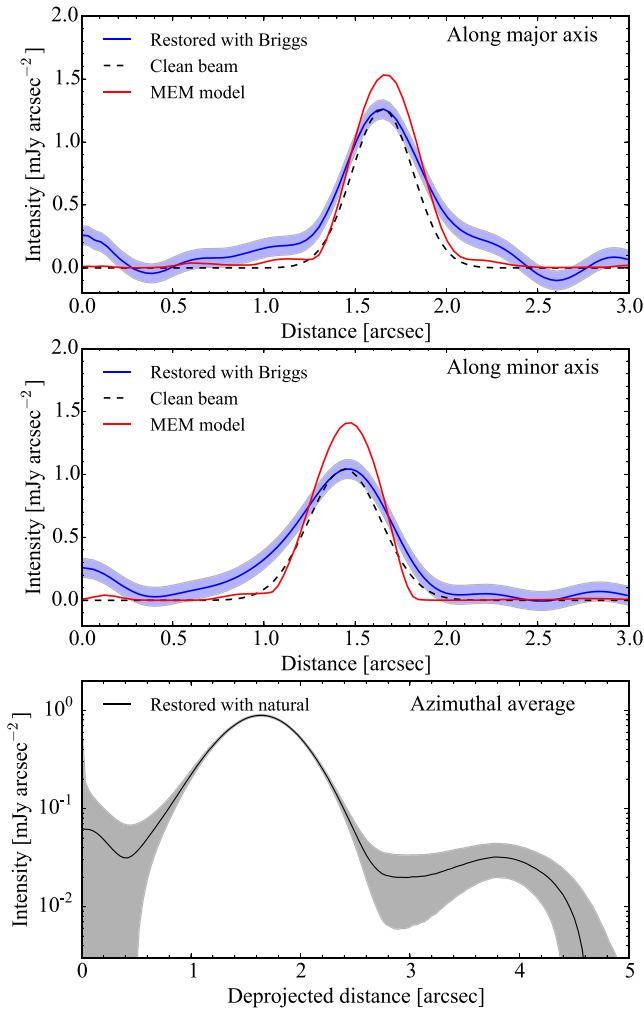
Figure 2. Intensity radial profiles of the dust continuum versus distance to the star along the major (top panel) and minor axis of the disc (middle panel). In the bottom panel, we present the mean intensity at all azimuths versus the deprojected distance to the star. The red, blue, black dashed and black continuous lines represent the MEM model, Briggs map, projected Briggs Clean beam and natural map, respectively. The blue and grey areas represent the 68 per cent and 99.7 per cent confidence regions, respectively.
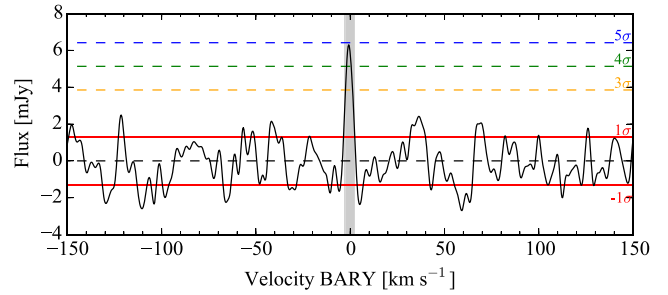

Figure 3. Continuum-subtracted integrated spectrum inside an elliptic mask of minimum and maximum semimajor axis of 1.4 and 2.1 arcsec, and oriented as the dust continuum ring. The original spectrum was smoothed with a Gaussian kernel with standard deviation of four channels. The horizontal lines represent ± 1, 3, 4 and 5σ levels. The grey region represents velocities between $-2.8 \, \mathrm{km \, s^{-1}}$ and $2.0 \, \mathrm{km \, s^{-1}}$ where the S/N is maximized. The velocities represent the Doppler shift with respect to 230.538 GHz in the Barycentric reference frame.

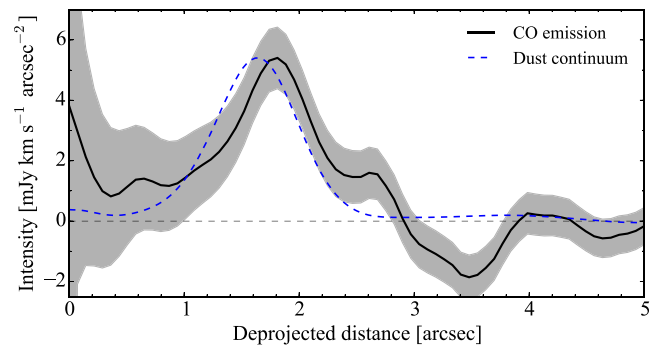

Figure 4. Mean intensity at all azimuths (black line) integrating from $-2.8 \, \mathrm{km \, s^{-1}}$ and $2.0 \, \mathrm{km \, s^{-1}}$ with respect to 230.538 GHz, in the Barycentric reference frame. The profile is extracted from the dirty map with natural weights of the continuum subtracted visibilities. The grey area represents the 68 per cent confidence region. In blue, we also present the mean intensity of the dust continuum presented in Fig. 2 in an arbitrary scale.

where no line emission is expected. The dirty map of the continuum subtracted data does not show any significant emission above 3σ which could be attributed to CO. With natural weights, we obtain a noise level of 1.0 mJy beam^{-1} per channel. To search for any low-level CO emission, we compute the total flux inside an elliptic mask and between a frequency or velocity range that we vary, both spatially and in frequency, to maximize the S/N of the integrated flux. The S/N is maximized inside an elliptic mask of minimum and maximum semimajor axes of 1.4 and 2.1 arcsec (assuming the same orientation and aspect ratio as the main ring) and a velocity range of -2.8 to $2.0 \, \mathrm{km \, s^{-1}}$ (Barycentric reference frame). These parameters match the location of the main ring and the expected Doppler shift due to Keplerian rotation, i.e. $v_0 = 0.1 \pm 0.4 \, \mathrm{km \, s^{-1}}$ (Gontcharov 2006) and $v_{\mathrm{max}} = 1.9 \, \mathrm{km \, s^{-1}}$ for $M_\star = 1.36 \, \mathrm{M_\odot}$ (Lebreton et al. 2012). The spectrum extracted from the data cube inside the elliptic mask and smoothed with a Gaussian kernel is presented in Fig. 3. The horizontal lines represent ± 1, 3, 4 and 5σ levels. The line peak is $\sim 5\sigma$. The integrated flux where the S/N is

maximized is $30.1 \pm 5.4 \, \mathrm{mJy \, km \, s^{-1}}$ (5.6σ). Moreover, we find that the CO emission in the south-east and north-west side of the disc are consistent with being blue and redshifted, respectively. As the disc's north side is the brightest in scattered light due to forward scattering, we can infer that it is also the closest side. This implies that the disc is rotating clockwise in the sky.

In Fig. 4, we present the integrated intensity over the velocity range specified above and averaging at all azimuths. The grey area represents the 99.7 per cent confidence region. The CO line peaks at 90 ± 4 au (error = $0.5 \times$ beam semimajor axis $\times$ distance / (S/N)), close to the ring radius in the continuum, suggesting that gas and dust are co-located. This favours a secondary origin scenario, where the CO is being released from icy bodies in the disc. We study the azimuthal profile of the emission along the ring and we find no evidence for non-axisymmetry, similar to the dust continuum. In Section 3.2, we study the CO gas distribution by modelling the CO emission in the non-local thermodynamic equilibrium (LTE) regime, with different excitation temperatures and electron densities which act as the main collisional partner. Using an MCMC technique, we find constraints on the distribution of CO gas in the disc to quantify its similarity to the dust distribution.

3 DISC MODELLING

3.1 Dust continuum

To constrain the location of the millimetre-sized dust population, we compare the observations with an axisymmetric debris disc model in the visibility space. The dust density distribution is parametrized as a ring of radius r_0, with a Gaussian radial profile of width Δr (FWHM) and a Gaussian vertical profile with a scaleheight H (vertical standard deviation) or aspect ratio $h = H/r$:

$$\rho(r, z) = \rho_0 \exp\left[-\frac{(r - r_0)^2}{2\sigma_r^2} - \frac{z^2}{2H^2}\right], \quad \sigma_r = \frac{\Delta r}{2\sqrt{2\log 2}}. \quad (1)$$

For the dust optical properties, we use a mass-weighted mean opacity of astrosilicate grains with an internal density of 3.5 g cm^{-3} (Draine 2003). We assume a Dohnanyi-like size distribution with a power-law index of -3.5, and minimum and maximum grain size $a_{min} = 1.3\,\mu$m and $a_{max} = 1.0$ cm. These values were roughly estimated comparing the model and observed SED in an iterative procedure. The mass-weighted absorption opacity $\kappa_{abs} = 1.1$ cm^2 g^{-1} at 1.3 mm, computed using the 'Mie Theory' code written by Bohren & Huffman (1983). While (a_{min}, a_{max}), κ_{abs} and the derived total dust mass are highly dependent on our choice on the grain composition and size distribution, these assumptions have very little effect on the derived disc structure. A detailed study on the grain properties of this disc can be found in Lebreton et al. (2012). Synthetic images are computed using RADMC-3D[1] (Dullemond et al. 2015), while the corresponding visibilities were derived using our tool uvsim. The free parameters in our model image and visibilities are r_0, h, Δr, M_{dust}, PA, inclination (i) and RA- and Dec.-offset. The last two to account for astrometric uncertainty and disc eccentricity.

We use a Bayesian approach to constrain the different parameters of the ring model, sampling the parameter space to recover the posterior distribution with the public PYTHON module *emcee* that implements the Goodman & Weare's Affine Invariant MCMC Ensemble sampler (Foreman-Mackey et al. 2013). The posterior distribution is defined as the product of the likelihood function and the prior probability distribution functions for each parameter, which we assume are uniform. The likelihood function is defined proportional to $\exp[-\chi^2/2]$, where χ^2 is the sum over the squared difference of the model and measured visibilities, divided by the variance. In our priors, we impose a lower limit to h equivalent to 0.03. This value is consistent with the minimum aspect ratio expected in the absence of perturbing planets (Thébault 2009).

The posterior distribution of h, Δr and r_0 is presented in Fig. 5, while in Table 1, we summarize the best-fitting values extracted from the marginalized distribution. As we previously mentioned, the ring is marginally resolved in the radial direction with an expectation value $\langle \Delta r \rangle = 23.2 \pm 1.0$ au, where the uncertainty represents the standard deviation derived from the marginalized posterior distribution. The width of the ring can be well constrained with the assumption of a Gaussian radial profile, but as it is of the order of the beam size, a detailed analysis of the radial structure of the main ring is impossible with the current angular resolution. The width of the ring is significantly larger than in the Fomalhaut ring (Boley et al. 2012). This could be related to the age of the systems as well as any possible planet- or star–disc interactions in the case of Fomalhaut (Shannon, Clarke & Wyatt 2014; Faramaz et al. 2015). In agreement with the ring radius derived in Section 2, we find $\langle r_0 \rangle = 86.0 \pm 0.4$ au.

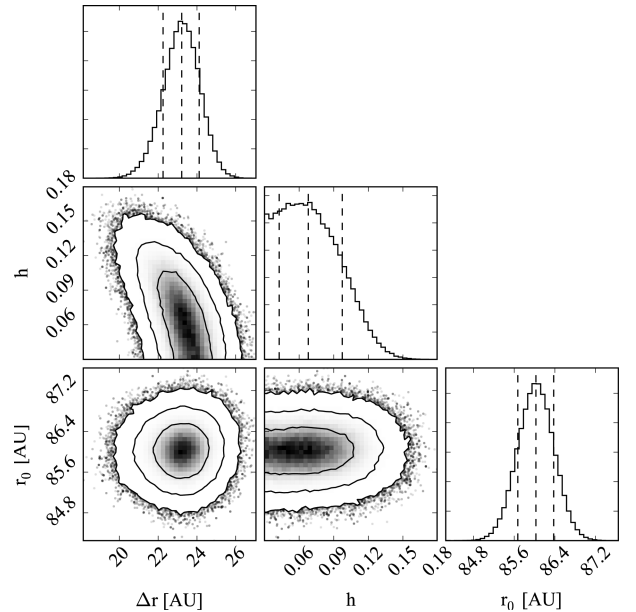[1] http://www.ita.uni-heidelberg.de/~dullemond/software/radmc-3d/

Figure 5. Posterior distribution of $h = H/r$, r_0 and Δr. The marginalized distributions of Δr, $h = H/r$ and r_0 are presented in the top, middle-right and bottom-right panel, respectively. The vertical dashed lines represent the 16th, 50th and 84th percentiles. Left-middle panel: marginalized distribution of h and Δr. Left-bottom panel: marginalized distribution of r_0 and Δr. Middle-bottom panel: marginalized distribution of r_0 and h. Contours correspond to 68 per cent, 95 per cent and 99.7 per cent confidence regions and the black dots to points of the MCMC outside the 99.7 per cent confidence region. This plot was generated using the PYTHON module *corner* (Foreman-Mackey et al. 2014).

Table 1. Best-fitting values for the dust continuum model. Median $\pm$ uncertainty based on the 16th and 84th percentile of the marginalized distributions.

Parameter	Best-fitting value
M_{dust} (M$_\oplus$)	0.422 ± 0.005
r_0 (au)	86.0 ± 0.4
Δr (au)	23.2 ± 1.0
h	0.07 ± 0.03
PA (°)	98.8 ± 1.4
i (°)	30.0 ± 0.7
RA offset (mas)	96 ± 5
Dec. offset (mas)	-42 ± 5

On the other hand, the scaleheight is not fully constrained. In principle, it should be possible to derive h from the ratio of the ring's width or surface brightness along the major and minor axis of the projected ring, causing h and Δr to be correlated. In addition to this, in our case, the estimation of h is limited as our observations only marginally resolve the ring's width. However, we can put a 99.7 per cent confidence upper limit of 0.14 for h. Both upper limit and best-fitting value (see Table 1) are consistent with the upper limit of 0.11 from Stark et al. (2014) and 0.09 from Schneider et al. (2006). The same figure shows that h and Δr are anticorrelated (see Section 4.9). In Section 4.9, we discuss about determining h in future observations and in other discs. The derived total dust mass in the main ring is 0.442 ± 0.005 M$_\oplus$. This value is highly dependent on our choice of dust internal density (3.5 g cm^{-3}) and for our assumed dust size distribution scales as $(a_{max}/1cm)^{0.5}$, noting that a_{max} is unconstrained. Moreover, the

uncertainty on the dust mass quoted above does not include the uncertainty on the absolute flux calibration, or the uncertainty on the stellar distance. Including these systematics, the uncertainty should be ∼12 per cent.

Our best axisymmetric model has $\chi^2_{red} \equiv \chi^2/(N - \nu - 1) = 1.54$, where N and ν are the number of independent measurements (visibilities) and free parameters and equal to 74 888 and 8, respectively. When we compare the χ^2 of our best axisymmetric model with the MEM model, we find a difference of 0.2 per cent. Hence, we conclude the continuum emission is consistent with an axisymmetric ring.

3.2 ^{12}CO (2–1)

To derive the CO gas distribution we follow a procedure similar to the dust continuum modelling in the previous section. We fit the data with an axisymmetric disc of gas with a density distribution parametrized similar to the dust density distribution, but with a fixed vertical aspect ratio h of 0.07 and fixed disc orientation, that corresponds to the best fit of the dust continuum (see Table 1). The gas is in Keplerian circular orbits with a fixed systemic radial velocity of 0.1 km s^{-1} in the Barycentric frame. Instead of simulating visibilities as in the dust continuum analysis, we fit the data with our gas models in the image space. The model images produced with RADMC-3D at different frequencies (tracing different radial velocities) are convolved with the dirty beam and then compared directly with the dirty map of the CO data, both corresponding to natural weights. This method is analogous to comparing model visibilities with gridded visibility data. The likelihood function is defined proportional to $\exp[-\chi^2/2]$, where χ^2 is the sum over the image and frequency space of the squared difference between the model and observed dirty map, divided by the variance, and taking into account the number of independent beams in the image and the correlation between adjacent channels in ALMA data. The free parameters in the MCMC are the CO gas mass (M_{CO}), ring radius (r_0) and FWHM of the ring (Δr).

However, the CO emission is not only constrained by the density distribution. Matrà et al. (2015) showed that LTE does not necessarily apply in the low-gas density environments of debris discs. Depending on the gas kinetic temperature and collisional partner densities, the derived gas mass can vary by orders of magnitude. Thus, to model the ^{12}CO (2–1) emission, it is necessary to include non-LTE effects, i.e. to solve the population levels including (de-)excitations through radiative process, where the cosmic microwave background (CMB) photons and dust thermal emission dominate the radiation field at 230 GHz, as well as through collisions. The similarity between the dust and gas distribution showed in Section 2.2 suggest that the CO is of secondary origin, e.g. produced by collisions between icy planetesimals that release volatile species such as CO or H$_2$O. This implies that the main collisional partner of CO molecules are electrons produced by carbon ionization and H$_2$O, which we neglect as is a much less efficient collider compared to electrons. However, we stress that the derived CO gas distribution and total mass (in both the extremes of radiation-dominated and LTE) are independent of the specific collisional partner, because it is the density of the partners that matters. That is, a different partner would yield a different range of values on the x-axis, but the same CO masses. We computed the CO-e$^-$ collisional rates using expressions described by Dickinson & Richards (1975). In Section 4.6, we discuss the origin of the CO gas. We also use as input our best-fitting model of the dust continuum to compute the dust contribution to the radiation field at 230 GHz.
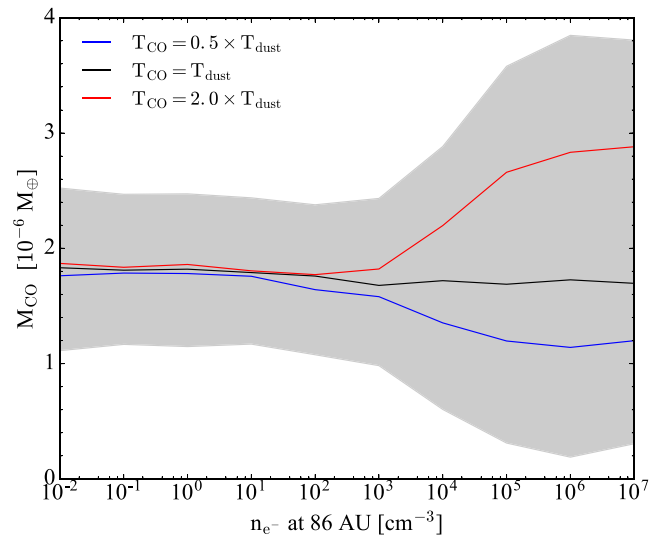

Figure 6. Best-fitting CO gas mass values obtained from our MCMC analysis using different kinetic temperatures and electron densities ($n_{e^-}^0$, main collisional partner). The blue, black and red lines correspond to kinetic temperatures equal to 0.5, 1 and 2.0 times the dust temperature in the disc, respectively. The grey area represents the 68 per cent confidence region with gas temperatures ranging between 0.5 and 2.0 times the dust temperature.

We consider different kinetic temperatures ranging from half to twice the dust temperature derived in the previous section (50 K at the ring radius). The electron density is defined as $n_{e^-}(r) = n_{e^-}^0 (r/86 \text{ au})^{-1.1}$, where the power-law index was assumed equal to the one derived for β Pic (Matrà et al., in preparation). We vary $n_{e^-}^0$ between 10^{-2} and 10^7 cm^{-3} to cover from the radiation-dominated regime to LTE. Scattered light images suggest that the north-east side of the disc is the closest as it is brighter in scattered light because of forwards scattering; thus, if the CO is in Keplerian rotation, we should be able to determine the direction at which the CO moves in the sky. Hence, we consider models of the disc rotating clockwise as well as anticlockwise. We find a best fit with the gas rotating clockwise on the sky. The best model is five times more likely than the best anticlockwise model and 300 times more likely than no CO emission. In Section 4.1, we discuss the implications for the observed asymmetries in scattered light. Below, we concentrate only on the clockwise case.

In Fig. 6, we present the CO gas masses derived with our MCMC-modelling technique for different kinetic temperatures and electron densities. We find that our best-fitting value of M_{CO} can vary due to the uncertainty in the excitation temperature between $1.2 \pm 0.4 \times 10^{-6}$ and $2.9 \pm 0.9 \times 10^{-6}$ M$_\oplus$ in the worst case (LTE), while it is very well constrained around $1.8 \pm 0.6 \times 10^{-6}$ M$_\oplus$ in the radiation-dominated regime (low n_{e^-}). Recent ALMA observations of the β Pic disc suggest $n_{e^-}^0 \sim 10^2$ cm^{-3} (Matrà et al., in preparation), which for HD 181327 corresponds to a scenario very close to the radiation-dominated regime. In Fig. 7, we present the posterior distributions, assuming $n_{e^-}^0 = 10^2$ cm^{-3} and equal gas and dust temperatures. We find $M_{CO} = 1.8 \pm 0.6 \times 10^{-6}$ M$_\oplus$, $r_0 = 81^{+10}_{-9}$ au and $\Delta r = 48^{+17}_{-21}$ au. This model has a total flux of ∼18 mJy km s^{-1}, a CO peak density of ∼0.15 cm^{-3} and peak optical depth of ∼0.007. We also notice that when both gas and dust temperature are equal, the difference in the derived CO mass between the radiation dominated regime and LTE is negligible because the radiation in the ring is actually dominated by the dust thermal emission rather than the CMB, as it was found to be the case in the Fomalhaut debris ring
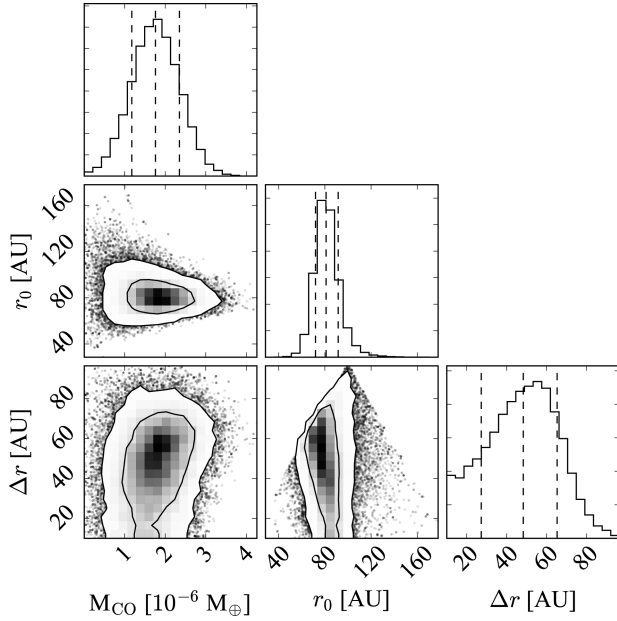
Figure 7. Posterior distribution of M_{CO}, r_0 and Δr of the CO disc. The marginalized distributions of M_{CO}, r_0 and Δr are presented in the top, middle-right and bottom-right panel, respectively. The vertical dashed lines represent the 16th, 50th and 84th percentiles. Left-middle panel: marginalised distribution of M_{CO} and r_0. Left-bottom panel: marginalized distribution of Δr and M_{CO}. Middle-bottom panel: marginalized distribution of r_0 and Δr. Contours correspond to 68 per cent, and 95 per cent confidence regions and the black dots to points of the MCMC outside the 99.7 per cent confidence region. This plot was generated using the PYTHON module *corner* (Foreman-Mackey et al. 2014).

Table 2. Best-fitting values for the CO model. Median $\pm$ uncertainty based on the 16th and 84th percentile of the marginalized distributions.

Parameter	Best-fitting value
M_{CO} ($M_\oplus$)	$1.2 \pm 0.4 \times 10^{-6}$–$2.9 \pm 0.9 \times 10^{-6}$
r_0 (au)	81^{+10}_{-9}
Δr (au)	48^{+17}_{-21}

(Matrà et al. 2015). We also find that the derived values of r_0 and Δr are independent of $n_{e^-}^0$ and the gas kinetic temperature. Table 2 summarizes the best-fitting values of the CO distribution.

The radius of the CO ring matches with the dust ring, confirming what we found averaging the data in Section 2.2, that gas and dust are co-located. Given the derived dust and CO densities, it is unlikely that the CO is self-shielded enough to avoid the photodissociation due to the ISM radiation field, which occurs in a time-scale of ~ 120 yr (Visser, van Dishoeck & Black 2009, see discussion in Section 4.6). This implies that the CO must be replenished and produced in the main ring; therefore, we conclude that the CO is of secondary origin and released by icy bodies. In Section 4.6, we discuss its origin. We also find that the CO ring could have a radial width similar to the dust distribution, although it is not very well constrained.

In Fig. 8, we compare the model spectrum with the spectrum extracted from the dirty map only integrating over the south-east half of the disc for negative radial velocities, and over the north-west half of the disc for positive radial velocities. With this approach, we obtain an integrated flux of 21.8 ± 4.3 mJy km s^{-1}, matching
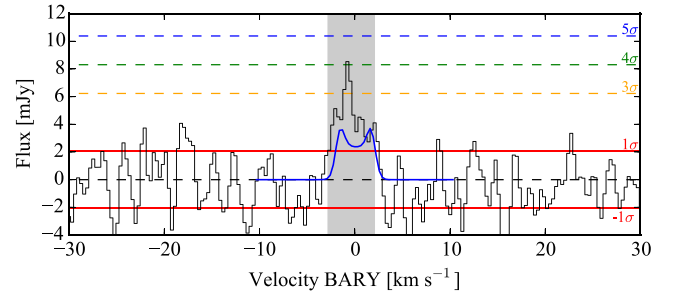

Figure 8. Blue line: model spectrum. Black line: continuum-subtracted integrated spectrum inside an elliptic mask of minimum and maximum semimajor axis of 1.4 and 2.1 arcsec, and oriented as the dust continuum ring. The horizontal lines represent ± 1, 3, 4 and 5σ levels. The grey region represents velocities between -2.8 km s^{-1} and 2.0 km s^{-1}. The velocities represent the Doppler shift with respect to 230.538 GHz in the Barycentric reference frame.

our best-fitting model and still consistent with the integrated flux presented in Section 2.2 (30.1 ± 5.4 mJy km s^{-1}) within the uncertainties. The model spectrum matches roughly the observed CO line profile.

4 DISCUSSION

4.1 Axisymmetry

In Section 3, we analysed the observations assuming an axisymmetric disc, however, Stark et al. (2014) found large-scale asymmetries consistent with either a recent catastrophic disruption of a large body or disc warping due to interactions with the ISM. Fig. 9 shows the best axisymmetric ring model image (a), the dirty map of the residuals when the best model is subtracted from the observed visibilities using natural weighting (b), and when the best double ring model is subtracted (c, see the section below). The map of residuals of a single ring is consistent with pure thermal noise without any peak intensity greater than 3σ along the main ring or where scattered light observations suggested an increase in the optical depth (black contours). The same image shows the two compact sources at ~ 8 arcsec N and 9 arcsec SW from the star described in Section 2.1. We can put an upper limit on any fractional enhancement of emission in the millimetre of ~ 10 per cent, which is lower than the asymmetries derived in scattered light (10–42 per cent). This can be translated to a mass upper limit of any dust density enhancement of 5×10^{-3} $M_\oplus$ beam^{-1} (~ 3 Pluto mass), assuming the dust composition and grain size distribution ($a_{max} = 1.0$ cm) described in Section 3. This mass upper limit scales roughly as $(a_{max}/1$ cm$)^{1/2}$ with the Dohnanyi-like size distribution, as noted in Section 3.1.

In a giant collision scenario, the small dust produced from the collision would initially form a trailing outward-propagating spiral structure due to radiation pressure that would orbit the star (Kral, Thébault & Charnoz 2013). After one orbit, the fragments would collide again in the 'pinch point' and would continually produce new debris in this region where the density is higher. The small dust produced by collisions would form a leading outward-propagating spiral structure from the pinch point as it is affected by radiation pressure (Jackson et al. 2014), and we would expect the millimetre-sized dust distribution to be narrower at the collision point, increasing the surface brightness. In addition, such a collision would produce a CO excess that would extend from the collision point, along the ring in the direction of motion as far as it can spread in
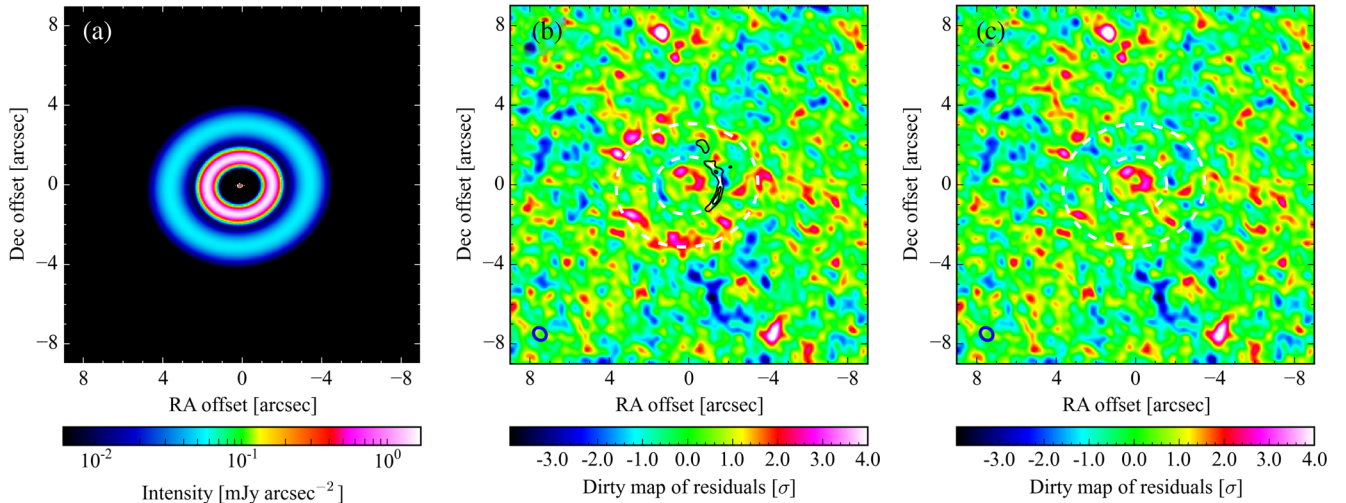
Figure 9. (a) Synthetic model image of the best-fitting model with two rings at 220 GHz. (b) Dirty map of the residuals of the best-fitting model with a single ring corresponding to natural weighting. The black contours represent the optical depth deviations from a uniform disc derived from *HST* images (Stark et al. 2014, left panel, Fig. 1). (c) Dirty map of the residuals of the best-fitting model with two rings corresponding to natural weighting. The white dashed contours in panels (b) and (c) correspond to radius of the main and second ring of the best-fitting two rings model. The Clean beam is represented by a blue ellipse (0.67 arcsec × 0.58 arcsec) in the bottom-left corner. The *x*- and *y*-axes indicate the offset from the stellar position in RA and Dec. in arcsec, i.e. north is up and east is left.

∼120 yr at which point is photodissociated, as the disc is optically thin, similar to the case of β Pictoris (Dent et al. 2014; Jackson et al. 2014).

Such features are not present in the millimetre continuum, nor in the CO emission. In Sections 2.2 and 3.2, we found that the CO and, thus, all the debris rotates clockwise in the sky. This has strong implications for the interpretation of the asymmetries in scattered light that extend outwards in an anticlockwise direction, forming a trailing spiral. The giant collision scenario could only explain the asymmetry if the collision has occurred in the last 4×10^3 yr or five orbits; thus, very unlikely. An alternative explanation of the asymmetry in scattered light could be that the disc is being warped by ISM interactions as suggested by Stark et al. (2014) or that the excess is being produced by a large body releasing small dust (e.g. Rappaport et al. 2014), in which case the asymmetric structure would form a trailing spiral of small grains that would orbit the star in clockwise direction.

4.2 Extended emission

Even though we model the disc as a single ring, we detect emission that extends at least to 4 arcsec (see Section 2.1). This emission is recovered both at the east and west side of the disc with no significant differences, and using our image synthesis method as well as using the Clean algorithm. Moreover, it appears in the residuals presented in Fig. 9(b). Assuming the same dust composition and grain size distribution as in the original ring, we model it with a second component in the dust density distribution. We find that this emission can be fitted by a power-law surface density distribution, that starts in the main ring with a surface density 25 times lower and that decreases as r^{-1}. An alternative is to add a second ring, in which case we find that the observations are best fit with a second ring of radius ∼185 au, FWHM ∼ 76 au and peak surface density 25 times lower than the maximum of the main ring. In both alternative models, we obtain a total flux of 8.6 ± 0.4 mJy and a dust mass of ∼0.57 ± 0.04 M⊕, assuming the same grain size distribution for the two components, an assumption which, as noted above, has significant influence on the derived dust mass. The flux

uncertainty does not consider the uncertainty on the absolute flux calibration (∼10 per cent). Fig. 9(c) shows the residuals when the double ring model is subtracted, obtaining a map with pure thermal noise. The origin of this emission could be dust on eccentric orbits produced in the main ring from eccentric planetesimals, or even primordial dust from the protoplanetary disc phase as this is a young system (∼23 Myr). This extended component could be related to the change in slope of the derived surface density near 150 au in scattered light (see fig. 9 in Stark et al. 2014). Deeper ALMA observations at a different wavelength or even Atcamaca Compact Array (ACA) observations coupled with detailed modelling are necessary to conclude about its origin. If the dust surface density distribution has a local minimum between 2 and 4 arcsec, this could be evidence of a perturbing planet orbiting in the gap or on a highly eccentric orbit (Pearce & Wyatt 2015).

4.3 Dust size segregation

From our MCMC analysis and the fit of an ellipse to the intensity maxima along the ring, we find that its radius is 86.0 ± 0.4, significantly smaller than at optical wavelengths ($r_0 = 90.5 \pm 1.1$). On the other hand, the distribution of small and millimetre grains overlaps. The main ring of millimetre grains extends roughly from 63 to 110 au, while the small dust is found roughly from 70 au and beyond 200 au. The difference in peak radius of 4.5 ± 1.2 au reveals grain size segregation. Due to radiation pressure, small dust grains released from larger bodies on circular orbits should be put on eccentric orbits with larger semimajor axes that depend on the grain sizes. The net effect is that the larger grains traced at millimetre wavelengths should remain in almost circular orbits at the radius of the parent planetesimal belt, while the spatial distribution of small grains shifts to larger radii (see Thébault & Wu 2008, for detailed modelling). The same segregation has been proposed for other debris discs, e.g. in au, Microscopii Strubbe & Chiang (2006) suggested a parent planetesimal belt at a specific radius to explain the surface brightness profile from scattered light images. This was later corroborated by millimetre observations (MacGregor et al. 2013).

4.4 Collisional time-scales

Rough estimates of the time-scale at which mass is being lost ($\dot{M}$) from planetesimals in the steady state collisional cascade can be made under the following assumptions: (1) the particles in the disc have small mean eccentricities and inclinations (*e* and *I*) equal to 0.05; (2) the relative velocities between particles is equal to $v_K(1.25e^2 + I^2)^{1/2}$ (valid for Rayleigh distributions of *e* and *I*; Lissauer & Stewart 1993; Wetherill & Stewart 1993); (3) planetesimal strengths ($Q_D^\star$) independent of size and equal to 230 J kg^{-1} (appropiate for km-sized weak ice bodies, Benz & Asphaug 1999; Wyatt & Dent 2002). Constant $Q_D^\star$ leads to a universal particle size distribution with a power-law index of −3.5, consistent with our assumptions in Section 3.1. Under these assumptions and using equations (15) and (16) from Wyatt (2008), we find $\dot{M} \sim 3$ M$_\oplus$ Myr^{-1}. By equating the collisional lifetime of bodies of different size with the age of the system (23 Myr), we also infer a maximum planetesimal size in the collisional cascade (D$_c$) of at least 1.8 km in diameter. Larger planetesimals may be present, but they would not yet have collided, thus they do not contribute to the collisional cascade. The collisional lifetime scales with the size of the body, D$_c$, roughly as (D$_c$/1.8 km)$^{0.5}$. We can then extrapolate this to obtain a collisional lifetime of mm-sized grains of 24 × 10^3 yr (~34 orbits).

Note that this collision time-scale is broadly consistent with equation (16) in Wyatt et al. (1999), given the different assumptions for these calculations. This emphasizes that the collisional lifetime of the mm-sized grains is set by the cross-sectional area in small grains, which is relatively well constrained from the observations, and is not dependent on the details of the collisional lifetimes of the largest objects discussed above.

4.5 Eccentric ring?

In our analysis, we also found that the ring centre is offset by 96 ± 5 mas in RA and −42 ± 5 mas in Dec. with respect to the phase centre, which was centred at the expected stellar position at epoch. However, the offset is within the astrometric rms of ALMA (~0.1 arcsec; private communication with ALMA helpdesk). An upper limit for the eccentricity of the ring can be estimated using a 3σ astrometric error of 0.3 arcsec. This results in an eccentricity upper limit of 0.18, consistent with the eccentricity of 0.02 ± 0.01 measured by Stark et al. (2014).

4.6 CO origin

We found that the CO is co-located with the dust, with no evidence for non-axisymmetry and with a radial extension consistent with the width of the main ring, although not well constrained. Given the CO derived mass and limits, we can estimate a vertical and radial column density of about 10^{13} and 10^{14} cm^{-2} depending on the gas kinetic temperature and electron densities (see Section 3.2), which implies a CO self-shielding coefficient of ~0.6–0.8 (Visser et al. 2009) (low self-shielding) and a photodissociation time-scale of ~150–200 yr due to the interstellar radiation field (see details in Matrà et al. 2015). Even if we assume that the CO is primordial and there is 10^4 times more H$_2$ than CO, the column density is still too low to shield the CO. Hence, the CO gas must have been produced recently and is probably continually replenished through destructive collisions or photodesorption of icy planetesimals, i.e. it has a secondary origin. Furthermore, given that the CO cannot exist for an orbital period at these distances (680 yr at 86 au), the majority of detected CO must be produced roughly axisymmetrically throughout the disc ring.

If we compare the derived CO mass with other debris discs with CO gas detected and of secondary origin (49 Ceti and β Pic; Dent, Greaves & Coulson 2005; Dent et al. 2014, respectively), we find that for HD 181327 M_{CO} is at least an order of magnitude lower. Moreover, the CO/dust mass ratio is within 3–7 × 10^{-6} in HD 181327, two orders of magnitude lower compared to β Pic (CO/dust mass ratio ~3 × 10^{-4}). The difference could be in the host star as 49 Ceti and β Pic are A stars, which could naturally favour the release of volatiles due to stronger radiation environments.

4.7 Cometary composition

In Section 4.4, we derived the mass-loss rate from planetesimals ($\dot{M}$), and in Section 4.6, we determined that the CO must be of secondary origin. Assuming that the mass of CO present in gas phase is in steady state, we can derive the CO ice mass fraction f_{CO} of planetesimals as a function of $\dot{M}$ and the photodissociation time-scale of CO τ_{co}. In steady state, we expect $f_{CO} \times \dot{M} = M_{CO} \times \tau_{co}^{-1}$, thus

$$f_{CO} = 3.4 \times 10^{-3} \left(\frac{M \int_{CO}}{1.8 \times 10^{-6} M_\oplus} \right)$$

$$\times \left(\frac{\dot{M}}{3 M_\oplus Myr^{-1}} \right)^{-1} \left(\frac{\tau_{co}}{175 \, yr} \right)^{-1}. \quad (2)$$

This value could vary from 3 × 10^{-3} to 6 × 10^{-3} due to systematic uncertainties in M_{CO} and $\tau_{co}(M_{CO})$. Moreover, the value of $\dot{M}$ is highly dependent on $Q_D^\star$ which could vary between 200 and 10^4 J kg^{-1} for km-sized bodies, making f_{CO} range between 3 × 10^{-3} and 0.11. Another big uncertainty is that an important fraction of CO could be also a product of CO_2, released from icy bodies and that photodissociates in a shorter time-scale of ~30 yr (Hudson 1971; Lewis & Carver 1983), or produced by CO_2 ice photodesorption. Thus, the CO ice fraction above can be interpreted as CO+CO_2 ice mass fraction of planetesimals. The net effect is that f_{CO+CO_2} is probably between 0.3 per cent and 16 per cent which is consistent with the CO+CO_2 abundances in Solar system comets (CO+CO_2 mass fraction of 3–27 per cent; Mumma & Charnley 2011). If the planetesimals have an ice to rock fraction similar to the Solar system of about unity, we can extrapolate and obtain an (CO+CO_2)/H$_2$O ice abundance ratio between 0.4 and 18 per cent. We stress that the CO and CO_2 production rate does not depend on the unknown mechanism that is releasing CO, as it will always be limited by the destruction rate of icy solids that sublimate CO or expose an icy surface.

4.8 Dust-gas interactions

The origin of the ring-like morphology of the HD 181327 disc is unclear. Lyra & Kuchner (2013) showed that dust–gas interactions can be non-negligible in debris discs and produce instabilities that shape the dust and gas distribution in narrow ring-like structures. These instabilities arise if: the dust stopping time τ_f is in the range of 0.1–10 × 1/Ω_K, with Ω_K the Keplerian rotation frequency, and dust to gas ratio $\epsilon \lesssim 1$. To ascertain if this could explain the dust distribution in the HD 181327 debris disc, we need to estimate τ_f and ϵ. A reasonable value for the stopping time as a function of the grain size can be obtained using the CO gas mass derived in our modelling, i.e. $M_{CO} = 1.2 \times 10^{-6}$–$2.9 \times 10^{-6} M_\oplus$, and if we assume: (1) the gas is dominated by CO, H$_2$O and their photodissociaton products; (2) the CO/H$_2$O ice mass ratio in planetesimals derived above (0.4–18 per cent); (3) the C/CO abundance ratio is ~100, the

same as in β Pic (Roberge et al. 2006). Under these assumptions, we find a total gas mass that could vary between 6×10^{-4} and $0.04 \, M_\oplus$.

The stopping time defined as $\tau_s = m v_{rel}/F_{drag}$ can be estimated considering the Epstein drag force that gas exerts on dust grains. We approximate the dust grain velocities with the same expression for the relative velocities presented in Section 4.4. The gas drag force depends on the gas density, gas kinetic temperature (T_k) and the grain size (a_d). The first can be derived assuming a gas density distribution proportional to the dust density distribution, while the second is assumed to be close to the mm-dust dust grain temperature in the ring ($\sim$50 K). Finally, we obtain

$$\tau_s \simeq 3 \times 10^3 \left(\frac{M_{gas}}{0.04 \, M_\oplus} \right)^{-1} \left(\frac{a_d}{1 \, mm} \right) \left(\frac{T_k}{50 \, K} \right)^{-1/2} \Omega_K^{-1}. \quad (3)$$

Thus, for mm-sized particles, $\tau_s \gtrsim 3 \times 10^3 \Omega^{-1}$, much longer than the necessary to trigger the instability. Moreover, the stopping time is even longer than the collisional lifetime calculated in Section 4.4 ($\sim$34 orbits). Only for grains at the bottom of the collisional cascade, with sizes $\lesssim 10 \, \mu m$, the stopping time is in the range where the instability could be triggered. The dust-to-gas mass ratio of grains smaller than $10 \, \mu m$ is of the order of unity. However, given that this instability does not apply to the mm-sized grains, and the distribution of micron-sized grains is consistent with being derived from the mm-sized grains, with any differences in their distribution attributable to radiation pressure without the need for the photoelectric instability, we conclude that this instability does not necessarily play a significant role in this disc. Furthermore, the collisional lifetime of μm-sized grains can be obtained using the fractional luminosity of the disc (Wyatt et al. 1999), which translates to $\sim$5 orbits, while the time-scale for the instability to occur is tens of orbital periods (Lyra & Kuchner 2013).

4.9 Scaleheight

We showed that ALMA observations can be useful to measure or constrain the vertical mass distribution in discs, even for non-highly inclined discs. Moreover, the dust thermal emission is not dependent on the scattering phase function, which hinders scaleheight estimates from scattered light observations. In the case of HD 181327, we found an upper limit for h consistent with previous observations. As h is directly related to the mean orbital inclination relative to the disc mid-plane, measurements of it at (sub)millimetre wavelengths can be a powerful tool for identifying perturbing massive bodies, e.g. planets on inclined orbits stirring the disc vertically.

To illustrate why ALMA observations can constrain h in narrow discs, we study the brightness profile at a given radius of model disc observations with different h, Δr and i. For a given surface density profile, different h's result in different azimuthal intensity profiles due to changes of the optical depth in the line of sight. For a narrow ring, higher values of h make the disc brighter at the ansae compared to the regions close to the disc minor axis. This is shown in Fig. 10 where we plot intensity profiles, normalized at the disc ansa (PA $= 90°$), versus position angle obtained from simulated ALMA cycle 3 observations. We used as input image our best-fitting ring model and we vary h and Δr. The equivalent angular resolution of the simulated observations is $\sim$0.25 arcsec. The upper panel corresponds to a disc inclination similar to HD 181327 (30°), while the lower panel to a general disc inclined by 70°. Based on the curves of three reasonable values of h, we find that the S/N required to determine the scaleheight is extremely dependent on the
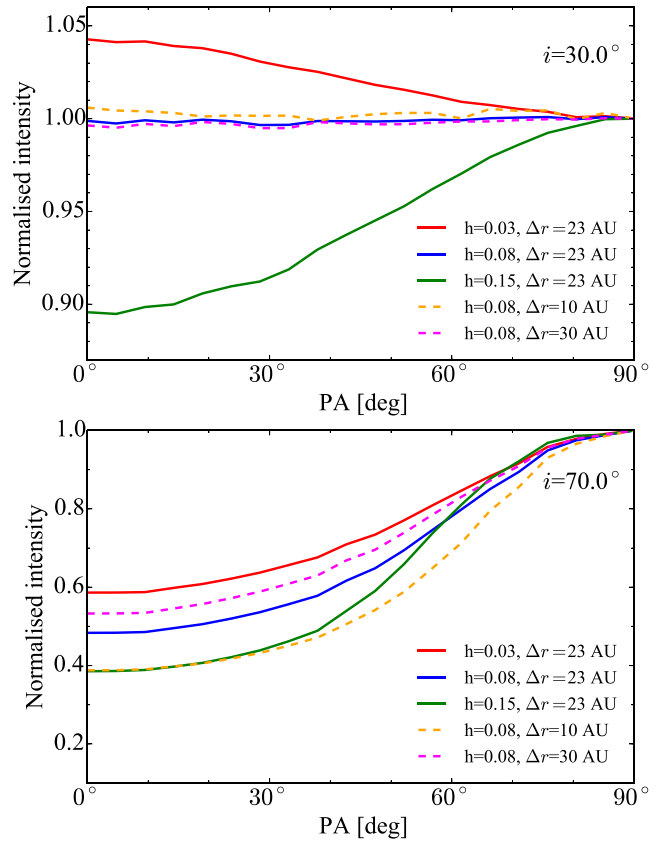

Figure 10. Intensity profiles along the ring projected ellipse on sky obtained from simulated Clean images without noise and using our best-fitting ring model. The values are normalized to the intensity at the ring semimajor axis (PA $= 90°$). The upper panel corresponds to a disc inclined by 30°, while the lower to 70°. In red, blue and green lines, we present three different profiles for disc aspect ratios of 0.03, 0.08 and 0.15 with Δr fixed to 23 au, while in dashed lines, we present profiles varying h and Δr.

disc inclination. For example, if we compare the profile of $h = 0.08$ and 0.03, the largest difference in the normalized intensity profiles is $\sim$4 per cent at PA $= 0°$ and $\sim$10 per cent when comparing $h = 0.08$ and 0.15. This can give a rough estimate of the required S/N to recover the original h in a real observation, i.e. S/N $\gtrsim 1/0.04 = 25$ to distinguish cases with h between 0.03 and 0.08, and S/N $\gtrsim 1/0.1 = 10$ to exclude h of 0.15 or higher. On the other hand, if the disc is inclined by 70° the S/N required to distinguished between the three cases would be $\gtrsim 1/0.2 = 5$. Hence, high S/N ALMA observations are fundamental to constrain the scaleheight of low inclined debris rings, and thus, the level of stirring of the debris.

Interestingly, changing Δr can produce a similar effect to the intensity profile. In the bottom panel, the dashed yellow line corresponding to $h = 0.08$ and $\Delta r = 10$ au has a similar profile compared with the case $h = 0.15$ and $\Delta r = 23$ au. However, Δr can be directly estimated measuring the width of the ring along the major axis, breaking this degeneracy. The anticorrelation between h and Δr mentioned in Section 3.1 that appears in Fig. 5 can be qualitatively understood as both h or Δr have an impact on the width of the ring projected in the sky.

Using the antenna configurations for cycle 3 provided in the CASA software, we simulate ALMA observations to estimate the necessary angular resolution to recover an aspect ratio h of 0.08 with an uncertainty less than 10 per cent of our best-fitting model for HD 181327, using our RADMC3D-MCMC approach. We find

that provided with a maximum projected baseline of 1.3 km at 220 GHz, i.e. an angular resolution of ~0.25 arcsec, and a S/N of ~50 along the ring, it would be possible to constrain $\langle h \rangle = 0.083 \pm 0.005$.

5 SUMMARY

We resolved the HD 181327 debris ring in dust continuum for the first time at millimetre wavelengths with an angular resolution of 0.47 arcsec × 0.36 arcsec and we detected ^{12}CO (2–1) emission for the first time in a debris disc around a solar-type star. Assuming an axisymmetric disc, we found that the dust continuum is best fit with a ring of radius 86 ± 0.4 au and width 23.1 ± 1.0 au. At this angular resolution, the vertical mass distribution is hard to constrain, but we were able to put an upper limit of 0.14 for the vertical aspect ratio h.

The ALMA observations are consistent with an axisymmetric ring and no significant residuals along the main ring remain after subtracting the best-fitting model to the continuum data. We also derived an upper limit for any dust overdensity along the primary ring. When we compared to previous *HST* observations at optical wavelengths, we found that the derived orientations of the disc on the sky are consistent, but the ring radius derived from our data is significantly smaller. This result is consistent with grain size segregation due to radiation pressure.

Additionally, we detected low-level emission that extends beyond the primary ring, consistent with either an extended halo of dust or a secondary ring. This result is robust against different image synthesis methods and is also recovered in the residuals of our best-fitting ring model. Deeper ALMA or ACA observations could help to study the origin of this emission.

We found that the CO is co-located with the dust, favouring a secondary origin scenario. Assuming an axisymmetric model, we model the CO emission in the non-LTE regime with different kinetic gas temperatures and collisional partner densities. With gas kinetic temperatures of 50 K and electron densities similar to the ones found in β Pic, the emission is best fit with a total CO gas mass of $1.8 \pm 0.6 \times 10^{-6}$ $M_\oplus$. In addition, we derived $CO+CO_2$ ice abundances in planetesimals and we found that they are consistent with the composition observed in Solar system comets. Furthermore, it is unlikely that the effect of hydrodynamics can affect the structure of the disc.

Finally, we showed that ALMA observations can be very useful to constrain the vertical distribution of discs. The S/N required is strongly dependent on the disc inclination in the sky, making it harder for discs close to a face-on orientation as HD 181327.

REFERENCES

Benz W., Asphaug E., 1999, Icarus, 142, 5
Bohren C. F., Huffman D., 1983, Absorption and Scattering of Light by Small Particles. Wiley, New York
Boley A. C., Payne M. J., Corder S., Dent W. R. F., Ford E. B., Shabram M., 2012, ApJ, 750, L21
Bryden G. et al., 2009, ApJ, 705, 1226
Casassus S., Cabrera G. F., Förster F., Pearson T. J., Readhead A. C. S., Dickinson C., 2006, ApJ, 639, 951
Casassus S. et al., 2013, Nature, 493, 191
Chen C. H., Fitzgerald M. P., Smith P. S., 2008, ApJ, 689, 539
Coughlan C. P., Gabuzda D. C., 2013, Proc. of 11th European VLBI Network Symposium & Users Meeting. Bordeaux, France
Dent W. R. F., Greaves J. S., Coulson I. M., 2005, MNRAS, 359, 663
Dent W. R. F. et al., 2014, Science, 343, 1490
Dickinson A. S., Richards D., 1975, J. Phys. B At. Mol. Phys., 8, 2846
Draine B. T., 2003, ApJ, 598, 1017
Dullemond C., Juhasz A., Pohl A., Sereshti F., Shetty R., Peters T., Commercon B., Flock M., 2015, RADMC3D v0.39, (available at http://www.ita.uni-heidelberg.de/dullemond/software/radmc-3d/)
Eiroa C. et al., 2013, A&A, 555, A11
Faramaz V., Beust H., Augereau J.-C., Kalas P., Graham J. R., 2015, A&A, 573, A87
Foreman-Mackey D., Hogg D. W., Lang D., Goodman J., 2013, PASP, 125, 306
Foreman-Mackey D., Price-Whelan A., Ryan G., Emily Smith M., Barbary K., Hogg D. W., Brewer B. J., 2014, triangle.py v0.1.1, (available at http://dx.doi.org/10.5281/zenodo.11020)
Gontcharov G. A., 2006, Astron. Lett., 32, 759
Heap S. R., Lindler D. J., Lanz T. M., Cornett R. H., Hubeny I., Maran S. P., Woodgate B., 2000, ApJ, 539, 435
Hillenbrand L. A. et al., 2008, ApJ, 677, 630
Hudson R. D., 1971, Rev. Geophys. Space Phys., 9, 305
Jackson A. P., Wyatt M. C., Bonsor A., Veras D., 2014, MNRAS, 440, 3757
Kalas P. et al., 2008, Science, 322, 1345
Kóspál Á. et al., 2013, ApJ, 776, 77
Kral Q., Thébault P., Charnoz S., 2013, A&A, 558, A121
Kuchner M. J., Holman M. J., 2003, ApJ, 588, 1110
Lebreton J. et al., 2012, A&A, 539, A17
Levanda R., Leshem A., 2010, IEEE Signal Process. Mag., 27, 14
Lewis B. R., Carver J. H., 1983, J. Quant. Spectrosc. Radiat. Transfer, 30, 297
Lissauer J. J., Stewart G. R., 1993, in Levy E. H., Lunine J. I., eds, Protostars and Planets III. Univ. Arizona Press, Tucson, p. 1061
Lyra W., Kuchner M., 2013, Nature, 499, 184
MacGregor M. A. et al., 2013, ApJ, 762, L21
Mamajek E. E., Bell C. P. M., 2014, MNRAS, 445, 2169
Marino S., Casassus S., Perez S., Lyra W., Roman P. E., Avenhaus H., Wright C. M., Maddison S. T., 2015, ApJ, 813, 76
Matrà L., Panić O., Wyatt M. C., Dent W. R. F., 2015, MNRAS, 447, 3936
Matthews B. C., Krivov A. V., Wyatt M. C., Bryden G., Eiroa C., 2014, in Beuther H., Klessen R. S., Dullemond C. P., Henning T., eds, Protostars and Planets VI. Univ. Arizona Press, Tucson, p. 521
Moór A., Ábrahám P., Derekas A., Kiss C., Kiss L. L., Apai D., Grady C., Henning T., 2006, ApJ, 644, 525
Moór A. et al., 2015, ApJ, 814, 42
Mumma M. J., Charnley S. B., 2011, ARA&A, 49, 471
Nilsson R., Liseau R., Brandeker A., Olofsson G., Risacher C., Fridlund M., Pilbratt G., 2009, A&A, 508, 1057
Nordström B. et al., 2004, A&A, 418, 989
Pantin E., Starck J.-L., 1996, A&AS, 118, 575
Pearce T. D., Wyatt M. C., 2015, MNRAS, 453, 3329
Perrin M. D. et al., 2015, ApJ, 799, 182

Rappaport S., Barclay T., DeVore J., Rowe J., Sanchis-Ojeda R., Still M., 2014, ApJ, 784, 40

Ricci L., Carpenter J. M., Fu B., Hughes A. M., Corder S., Isella A., 2015, ApJ, 798, 124

Roberge A., Feldman P. D., Weinberger A. J., Deleuil M., Bouret J.-C., 2006, Nature, 441, 724

Schneider G. et al., 2006, ApJ, 650, 414

Shannon A., Clarke C., Wyatt M., 2014, MNRAS, 442, 142

Stark C. C., Schneider G., Weinberger A. J., Debes J. H., Grady C. A., Jang-Condell H., Kuchner M. J., 2014, ApJ, 789, 58

Strubbe L. E., Chiang E. I., 2006, ApJ, 648, 652

Thébault P., 2009, A&A, 505, 1269

Thébault P., Wu Y., 2008, A&A, 481, 713

Torres C. A. O., Quast G. R., da Silva L., de La Reza R., Melo C. H. F., Sterzik M., 2006, A&A, 460, 695

van Leeuwen F., 2007, A&A, 474, 653

Visser R., van Dishoeck E. F., Black J. H., 2009, A&A, 503, 323

Warmuth A., Mann G., 2013, A&A, 552, A86

Wetherill G. W., Stewart G. R., 1993, Icarus, 106, 190

Wyatt M. C., 2008, ARA&A, 46, 339

Wyatt M. C., Dent W. R. F., 2002, MNRAS, 334, 589

Wyatt M. C., Dermott S. F., Telesco C. M., Fisher R. S., Grogan K., Holmes E. K., Piña R. K., 1999, ApJ, 527, 918

Zuckerman B., Song I., 2012, ApJ, 758, 77

Zuckerman B., Forveille T., Kastner J. H., 1995, Nature, 373, 494

APPENDIX A: POSTERIOR DISTRIBUTION OF DISC PARAMETERS

In Fig. A1, we present the posterior distribution of all the free parameters in the disc model of the dust continuum described in Section 3.1.
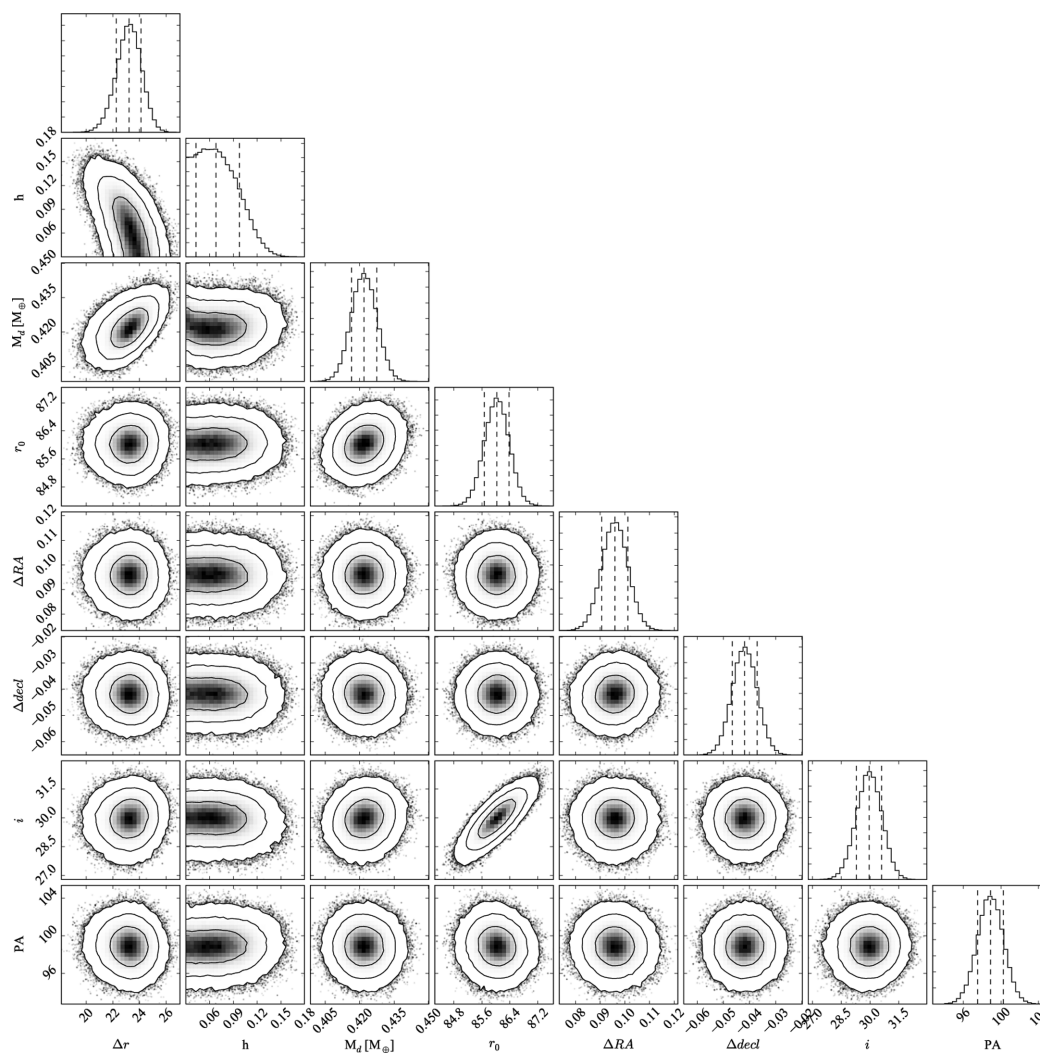
Figure A1. Posterior distribution of Δr, $h = H/r$, M_d, r_0, RA and Dec. offsets, i and PA. The 1D marginalized distributions are presented in the diagonal, while the 2D marginalized distributions are presented in in the bottom-left half. The vertical dashed lines represent the 16th, 50th and 84th percentiles. Contours correspond to 68 per cent, 95 per cent and 99.7 per cent confidence regions and the black dots to points of the MCMC outside the 99.7 per cent confidence region. This plot was generated using the PYTHON module *corner* (Foreman-Mackey et al. 2014).

This paper has been typeset from a TEX/LATEX file prepared by the author.